IOP PUBLISHING JOURNAL OF PHYSICS D: APPLIED PHYSICS

J. Phys. D: Appl. Phys. **43** (2010) 365204 (10pp) doi:10.1088/0022-3727/43/36/365204

Particle in cell modelling of the observed modes of a dc wire discharge

R Gueroult[1,2], P Q Elias[1], D Packan[1], J Bonnet[1] and J M Rax[2]

[1] ONERA Palaiseau, 91761 Palaiseau, France
[2] LPP, Ecole Polytechnique, 91128 Palaiseau Cedex, France

E-mail: renaud.gueroult@polytechnique.edu

Received 12 May 2010, in final form 22 July 2010
Published 25 August 2010
Online at stacks.iop.org/JPhysD/43/365204

Abstract

Low-pressure dc wire induced plasma sources exhibit two stable modes of discharge—constricted below a threshold pressure and diffuse above. Starting from experimental measurements, we conduct two-dimensional particle in cell (PIC) modelling of a dc low-pressure (10^{-4}–10^{-2} mbar), low-current (∼1 mA) wire discharge in helium. 2D PIC modelling is required to capture longitudinal non-uniformity of the diffuse mode. PIC simulations reproduce the two discharge modes. The voltage versus pressure curve obtained from simulations matches fairly well the experimental data, including the transition region. Discharge voltage dependence on pressure is analysed in consideration of electron impact ionization rates' evolution with energy. In light of the PIC findings, a model of the discharge mode transition based on the Child–Langmuir theory for ions is proposed. Confrontation with simulated data shows good agreement and validates the model for mode transition prediction. Simulations show that the diffuse mode is a space-charge-dominated regime.

(Some figures in this article are in colour only in the electronic version)

1. Introduction

A wire-induced plasma source (WIPS) is a type of low-pressure gas discharge. Low-pressure discharge specificity relies on the fact that the electron mean free path often exceeds the discharge chamber typical length scale, thus requiring a way of confinement. In the case of WIPSs, efficient confinement is achieved electrostatically [1], electrons being captured in the logarithmic potential generated between a cylindrical cathode and a positively biased wire anode centred inside the cathode. This technique is the direct transposition—reversed polarity—of the one used in the Kingdon [2] ion trap, and permits low pressure (∼10^{-5} mbar) gaseous discharge at very low applied voltage (∼1 kV) within a chamber a few centimetres in size.

Consequently, WIPSs have been used as an ion source for secondary emission electron guns [3], and their development has been pushed forward within this framework: versions of WIPS with multiple wires [4] and axial magnetic field [5] to increase their efficiency have been proposed. Nevertheless, those improvements are balanced by the increased weight and complexity of the system induced by the addition of magnets and/or wire tightening systems. Since then, whilst wire sources are widely used in electron guns, efforts to develop an understanding of the WIPS itself had been scarce. Most of the studies have been devoted to pulsed WIPS which can develop current density of about one ampere per centimetre length, being therefore a good candidate as ion source for the high-current electron gun [3, 6–8]. Recently, Makarov undertook both an experimental [9] and a 1D numerical study [10, 11] of a high-current pulsed WIPS and the temporal evolution of the discharge.

Experiments show that, depending on operating conditions, various modes of discharge are observed. This has been reported in various configurations: single [12] or multiple wires [13] at low pressure, single wire at higher pressure [14]. Low-pressure dc WIPS in the milliampere range, used for example in electron beam fluorescence (EBF) optical diagnosis [15] electron guns, exhibits two distinct modes of discharge. Apart Pigache's [12] remark that, in the high pressure mode, the cathode sheath length was of the same order as the planar Child–Langmuir length, to our knowledge, no thorough model of the dc low-pressure, low-current wire source was given. A better understanding of the main physical features of the wire

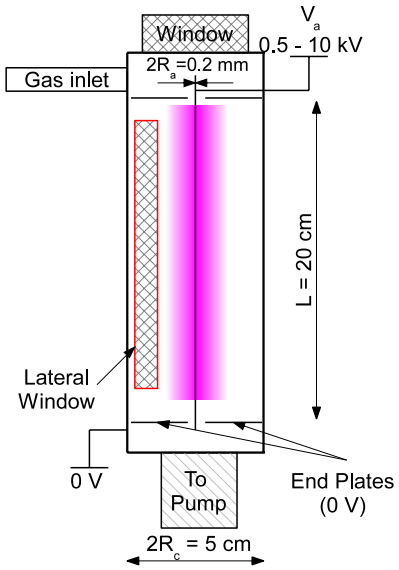

Figure 1. Experimental setup. The anode is a tungsten wire 0.1 mm in radius, the cathode is a stainless steel cylinder 2.5 cm in radius and 20 cm long. The vessel is filled with helium. Anode potential is $V_a = 0.5$–10 kV dc. End plates ensure longitudinal electrostatic confinement.

discharge would benefit EBF electron guns' optimization and development of dc WIPS-based technologies.

In this paper, we seek to examine the WIPS physics, and in particular its mode transition, in the light of an experimental characterization. We numerically investigate the operation of a dc low-pressure (10^{-4}–10^{-2} mbar), low-current ($\sim$1 mA) wire discharge which could typically be used in EBF electron guns. We limit our study to the single-centred wire configuration without applied magnetic field. To begin with, an experimental characterization of the wire discharge is conducted in section 2. Description of the specific features of our 2D particle in cell (PIC) code follows in section 3. PIC modelling validation is then achieved by confronting numerical results with experimental data in section 4. Finally, based on simulations microscopic outputs we propose macroscopic models of observed phenomenon in section 5.

2. Experimental characterization of the low-pressure WIPS

2.1. Experimental setup

Experimental measurements have been made on the setup sketched in figure 1. The cathode is made of a $R_c = 2.5$ cm inner radius, $L = 20$ cm length stainless steel cylinder. At one end of the cylinder, a silica window allows observation of the radial expansion of the discharge. Another window is installed laterally to monitor the longitudinal plasma development. The anode is a $R_a = 0.1$ mm radius tungsten wire placed on the axis of the cylinder. Grounded end plates at each end provide longitudinal confinement. These discs have an inner hole diameter of 6 mm.

The plasma source was directly mounted on a Pfeiffer HiCube turbo pump reaching an ultimate pressure of 6×10^{-7} mbar in measurement configuration. Measurements presented in this paper were done in helium, but Ne, Ar, Xe, NO, CO, CO_2 and air have been successfully tested. Incoming gas flow was controlled by a an input valve. In order to have reliable reading of the pressure, several pressure gauges were compared and cross calibrated: two Baratron capacitive gauges, one hot cathode Bayard–Alpert gauge and one Pfeiffer Compact Full Range gauge. Pressure resolution in that configuration was about 10^{-5} mbar.

Typical anode voltage (V_a) varies from 500 V to 10 kV depending on the gas type and pressure. Heinzinger LNC stabilized dc power generators were used. A +10 kV, 2 mA generator was used for low pressure measurements, whereas a +1200 V, 10 mA generator was used for higher pressure.

Voltage and current were recorded using a P6015A Tektronix high voltage probe and a Hall current probe, respectively, and displayed on a LeCroy 100 MHz oscilloscope. Current was measured at the power generator output.

2.2. Discharge modes

Two discharge modes are observed experimentally. These modes are similar to those described by Pigache [12] at higher currents. Figure 2 presents the discharge evolution with pressure.

At low values of pressure ($p \leqslant 10^{-2}$ mbar), the plasma glow is limited to a region close to the anode, but fully expanded longitudinally. Therefore, we refer to this mode as the *constricted* mode. When the pressure is decreased ($p < 2 \times 10^{-3}$ mbar), the wire becomes red hot, and discharge voltage curve diverges. According to Francis [16], the divergence of the discharge voltage with pressure decrease is symptomatic of an obstructed discharge. This behaviour combined with, as it will be shown later, the potential profile near the anode indicates that the constricted mode might be an obstructed discharge in a wire cylinder configuration.

On the other hand, when pressure is increased above the threshold value, the discharge switches to a *diffuse* mode. The transition is sudden, and a voltage drop of slightly less than a hundred volts is observed. The system exhibits hysteresis on mode transition, the transition occurring at slightly lower (respectively higher) pressure when decreasing (respectively increasing) the pressure. In the *diffuse* mode, the plasma glow fills the whole radial interelectrode volume but is limited longitudinally to a slice of a few centimetres. For a given pressure, the slice width increases with current, as shown in figure 3. In the diffuse mode, current increase is obtained at almost constant voltage, which is a characteristic feature of a normal glow discharge.

3. PIC modelling of low-pressure discharge

Longitudinal constriction of the discharge at the mode transition underlines the importance of 2D effects. It is therefore necessary to use a bi-dimensional model to simulate the wire discharge behaviour. Moreover, a Knudsen number well above one due to the low working gas pressure implies a PIC numerical modelling.

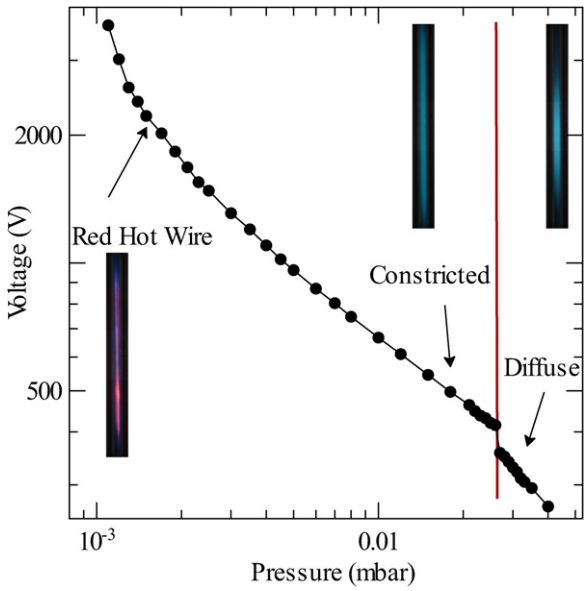

Figure 2. Voltage versus pressure curve for a 1 mA current. The *diffuse* mode is observed at high pressure, transition (red vertical line) occurs on decreasing the pressure and the *constricted* mode takes place. At lower pressure, the anode becomes red hot.

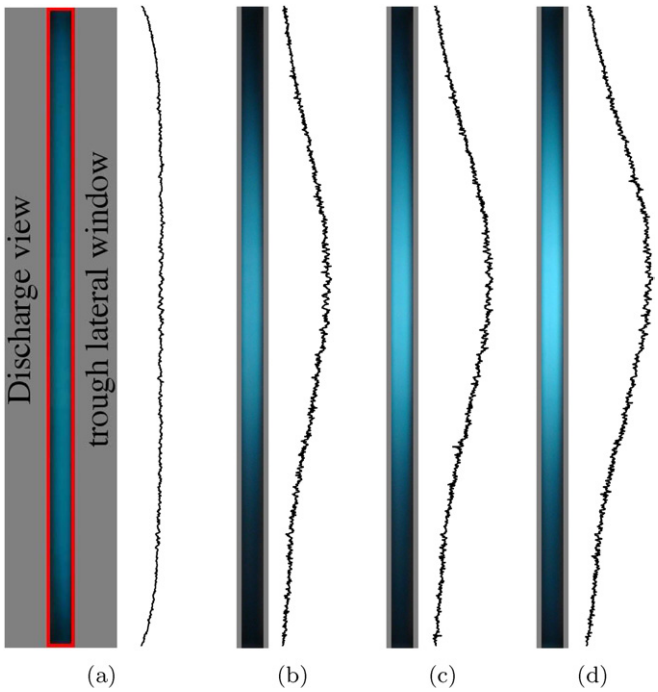

Figure 3. Discharge profile views through the lateral window. (*a*) Constricted mode $p = 1 \times 10^{-2}$ mbar, $I = 1$ mA; (*b*)–(*d*) diffuse mode ($p = 2.8 \times 10^{-2}$ mbar) longitudinal expansion with current for $I = 1$, 1.5 and 2 mA.

In a classical manner [17–19], a two-dimensional 2D3V (r, z) PIC code has been developed. Particles modelled are electrons, ions and fast neutrals. Fast neutral population is included mainly for secondary emission purposes. Indeed due to the high value of the charge exchange cross section in helium, depending on pressure conditions, fast neutral number density could be rather important and thus neutrals could play a role on secondary emission. Particle trajectories are computed using a Runge–Kutta fourth-order algorithm. The anode radius R_a being an order of magnitude smaller than the chamber radius R_c, a non-uniform cylindrical mesh has been used to minimize the number of cells. Nevertheless, it is strictly necessary to resolve properly the wire to compute high field gradients in this area and hence to integrate properly the particle trajectories.

Table 1. Active species—background gas collision processes modelled in the simulations. Corresponding cross section are from Hartmann *et al* [20], except for electron impact excitation taken from Stone *et al* [21].

Electron impact induced processes	
$e^- + He \rightarrow e^- + He$	Elastic
$e^- + He \rightarrow e^- + He^\star$	Excitation
$e^- + He \rightarrow 2e^- + He^+$	Ionization
Ion impact induced processes	
$He^+ + He \rightarrow He^+ + He$	Elastic
$He^+ + He \rightarrow He + He^+$	Charge exchange
$He^+ + He \rightarrow He^+ + He^\star$	Excitation
$He^+ + He \rightarrow 2He^+ + e^-$	Ionization
Fast neutral impact induced processes	
$He^f + He \rightarrow He^f + He$	Elastic
$He^f + He \rightarrow He^f + He^\star$	Excitation
$He^f + He \rightarrow He^f + He^+ + e^-$	Ionization

Despite the low working pressure, collisions are fundamental to model the discharge. Consequently, we implemented a complete Monte Carlo collision (MCC) module [19]. Collisions taken into account in the simulation are given in table 1. The corresponding cross sections are those gathered by Hartmann *et al* [20], an exception is made of electron impact excitation for which we used Stone's [21] data. Indeed, Hartmann *et al* [20] cross sections for this process differ significantly from standards [21]. Regarding the excitation process, only one excited level is taken into account, but the energy loss during the excitation process is computed randomly between the energy of the first excited level and the ionization energy. For a given collision process, energy distribution between all particles involved is computed by inverting the differential cross section $\sigma(E, \chi)$ for that collision [19, 22]. Gas-dependent fitting parameters for ionization processes are taken from Opal *et al* [23]. Null collision technique [24] has been implemented to speed up calculations.

Due to the low working pressure, collisions between active populations are neglected. Similarly, the low ionization fraction justifies the implementation of a fixed density background gas.

Secondary emission models are used for all three species' impacts on the electrodes. The processes involved for heavy particles are kinetic emission (ions, fast neutrals) and potential emission (ions) [25, 26]. For ion impact secondary electron emission at a few hundred electron volts, references for the fitting parameters are scarce in the literature. For example, Bohm and Perrin [27] give a value $\gamma_{He^+} \sim 0.25$ emitted electrons per incident ion at 350 eV whereas Szapiro *et al* [28] have $\gamma_{He^+} \sim 0.6$ at 500 eV, both for clean stainless steel. In addition, the secondary emission coefficient depends strongly

Table 2. Simulation conditions used for comparison with experimental discharge modes.

	Case A	Case B	Case C
Mode	Constricted	Diffuse	Diffuse
Pressure (10^{-2} mbar)	1.36	6.07	6.07
Current (mA)	1	1	2

on surface condition, this parameter being hardly known. Following Bohm and Perrin [27], simulations are made using

$$\gamma_{He^+} = 0.3, \qquad \gamma_{He^0} = 0.1 \tag{1}$$

as default values. The influence of those parameters will be analysed parametrically. Impacting electrons can be elastically or inelastically reflected or create true secondaries [29–31].

Depending on the plasma impedance, ideal voltage sources can induce instabilities. It is thus desirable to drive the plasma with an ideal current source. The anode potential evolves due to the cumulated effect of impacting particles and electrons drawn by the current source. The simulation runs until electrode currents have converged to a specified value.

4. Code validation: comparison with experiments

In order to validate the PIC code described in the previous section, test cases are run and results are confronted to experimental data. Simulations results are compared with experiments on two different levels. First, visual aspect and spatial properties of the simulated discharge are compared qualitatively with experimental pictures. Then, computed voltage versus pressure curve is examined in light of the experimental one.

4.1. Discharge modes: spatial properties

Three cases matching the experimental modes of discharge are numerically modelled. Working conditions of these cases are summarized in table 2. The first one corresponds to a constricted mode at a 1 mA discharge current (case A). The others are diffuse modes for 1 mA and 2 mA (cases B and C, respectively).

Figure 4 presents the Abel transform of the volumic excitation rate for the three cases. The Abel transform of the excitation rate is directly related to the emitted light and its comparison with observed glow is a good indicator. Simulations confirm the existence of a *constricted* mode of discharge where excitation is localized near the anode and uniform longitudinally. At higher pressure, for the same 1 mA discharge current, the excitation area increases radially and collapses longitudinally. The longitudinal expansion with current is well modelled by the simulations.

Longitudinal profiles of the Abel transform of excitation are plotted with profiles obtained from experimental pictures in figure 5. No correction has been made to the raw data, except a normalization of all simulated curves with a single coefficient equal to the ratio of the observed maxima over the simulated one for the 2 mA *diffuse* mode case. Relative levels of intensity

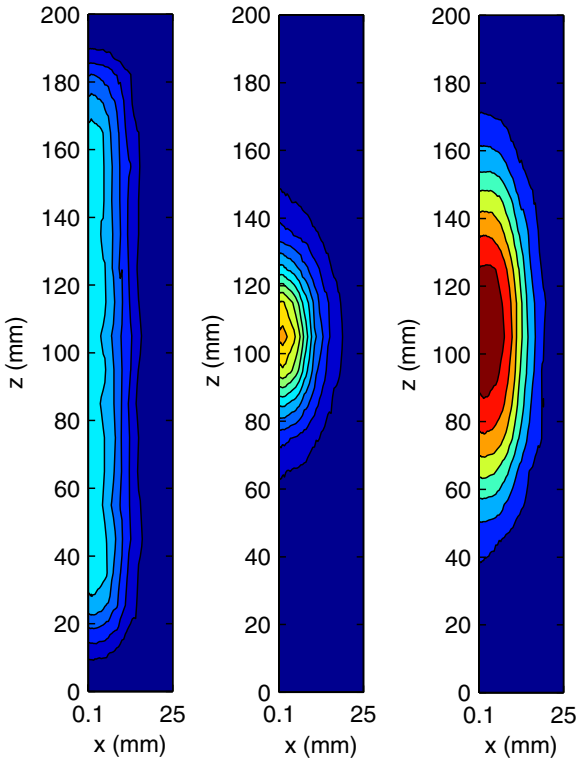

Figure 4. Simulated discharge modes: (*a*) constricted mode at 1 mA discharge current, $p = 1.36 \times 10^{-2}$ mbar (case A), (*b*) and (*c*) diffuse mode at $p = 6.07 \times 10^{-2}$ mbar for 1 mA and 2 mA discharge current, respectively (cases B and C).

for simulated and experimental data are almost equal, and shapes, although not exactly superimposed, are qualitatively identical. Indeed, simulated emission profile maxima are more peaked than the experimental ones. Reflected light—not modelled in our PIC code—is thought to contribute to the peak broadening. Indeed excitation produces photons with directions distributed equally on a solid sphere angle, and only a small fraction of it directly hit the camera detector. Another fraction of photons is diffused from the cathode surface and then possibly enter the camera detector. Diffusion can take place in areas far from the median plane, increasing in turn the signal on both sides of the excitation maximum.

4.2. Discharge voltage variation with pressure

The simulated discharge voltage versus pressure is plotted along with the experimental data in figure 6. The sharp transition observed experimentally between the two modes is found as well on the simulated curve. The voltage jump is well defined, and curve evolutions around the mode transition are very similar: computed curve slopes above and below the mode transition closely match the experimental ones. A discrepancy between simulated and experimental data is mainly present on the high-pressure region, where, as will be shown in the next paragraph, secondary emission coefficient value plays a role. For lower pressures, PIC results stick closely to the experimental ones, modelling properly the strong rise in discharge voltage with pressure decrease.

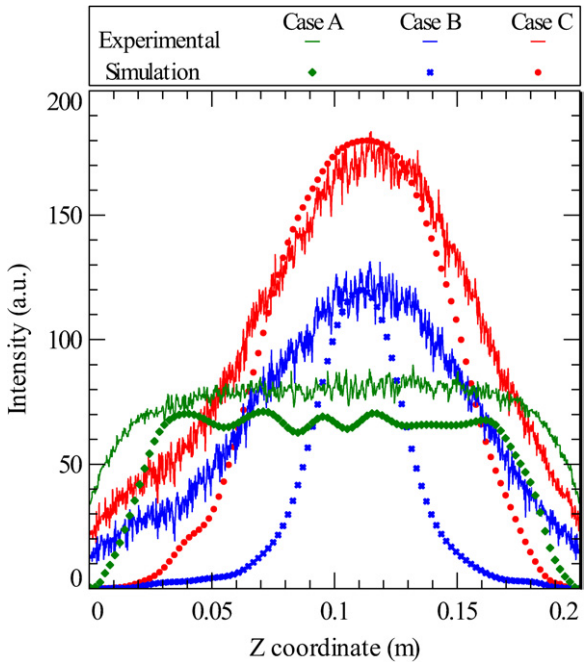

Figure 5. Simulated and experimental plasma longitudinal expansion profiles. Simulations conditions are summarized in table 2.

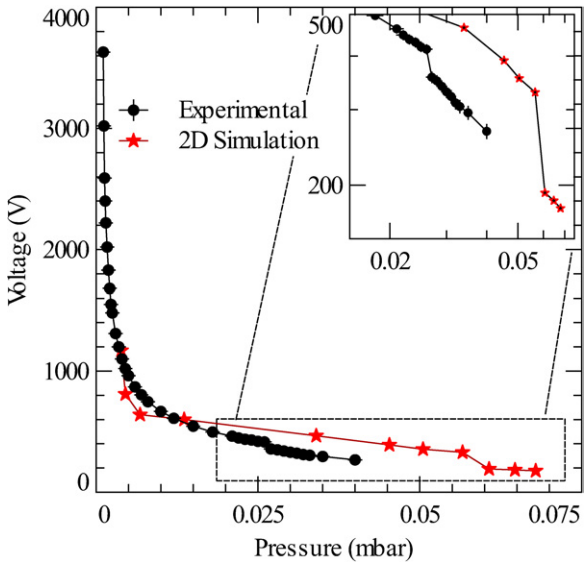

Figure 6. Experimental and simulated discharge voltage versus pressure for 1 mA current. Voltage jump of slightly less than hundred volts is observed on both curves.

4.3. Influence of secondary emission coefficients

As mentioned in section 3, constant secondary electron emission value for ion and fast neutral impact were used due to the lack of data in the literature. A parametric study was made to discriminate the influence of these coefficients on the simulations. Before any computational study, an analysis could be formulated as follows. Increasing secondary emission coefficients would lead to higher electron population number N_{e^-}, and in turn to higher ionization rate, yielding eventually a higher discharge current ($I > I_0$). On the pressure range considered, the plasma is resistive, meaning that the original I_0 discharge current can be obtained at lower voltage using higher value of γ. Moreover, the fraction of secondary electrons returning to the cathode increases with mean free path, thus dependence on γ should diminish with pressure decrease. Simulations made with $\gamma_{He^+} = 0.6$ validate this analysis: the transition occurs numerically at the same voltage $V \sim 330$ V despite of a drop in the mode transition pressure from $p_t = 6 \times 10^{-2}$ mbar for default γ_{He^+} value to $p_t = 4.4 \times 10^{-2}$ mbar. Influence of secondary emission on the voltage versus pressure curve given in figure 6 is hence mainly a shift to the left, the mode transition occurring then at lower pressure. This shift will be explained by the mode transition model proposed in section 5.

To summarize, secondary emission values tuning could diminish, if not remove, discrepancies between simulations and experimental data in terms of pressure of transition. Considering that secondary emission values do not change the fundamental behaviour—mode transition, spatial properties of the modes—of the discharge on the pressure range considered and that these coefficients are hardly predictable, no further attention has been paid to this phenomenon.

5. Discussion

Numerical results on the previous test cases justify the use of the code as a means to dig out microscopic data, e.g. ionization volumic rates or densities, to propose a macroscopic model of the discharge.

5.1. Model of the mode transition

Based on experimental measurements, Pigache [12] noted that the high pressure cathode sheath width was of the same order as the Child–Langmuir length computed for a helium ion current between planar electrodes. Makarov *et al* [9] used the same approach to describe one state of its pulsed wire discharge. Those analyses rely on the hypothesis that the discharge can be on first approximation considered as a unipolar current of helium ions. In order to extend Pigache's argument to the mode transition analysis, this hypothesis has to be justified at first.

When pressure is increased, the ion mean velocity decreases because of the lower discharge voltage and higher collision rate with the neutral background gas. Considering that the cathode current is mainly an ion current, in order to sustain a given current, the ion population number should increase to balance the velocity decrease. This way, the ion flux to the cathode remains constant. Due to charge exchange collisions, fast neutral population follows the ion population increase, until pressure reaches the threshold value. Beyond this limit, the fast neutral energy is limited as well by a lower discharge voltage and elastic collisions, and hence more and more fast neutrals are transferred back to the background gas population as pressure increases. Indeed neutrals are monitored as fast neutrals as long as their energy exceeds a given value, taken as a threshold for kinetic secondary emission on electrodes.

Simulation results presented in figure 7 confirm these variations. The ion population number is about ten times

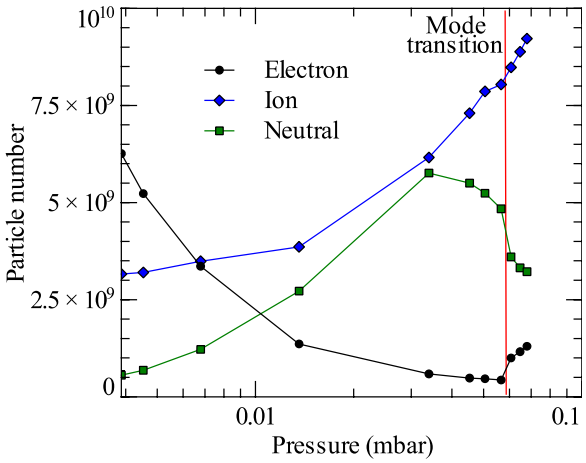

Figure 7. Evolution of electron, ion and fast neutral population numbers with pressure. Plasma is mainly made of ions at high pressure, whereas electron number increases strongly at lower pressures.

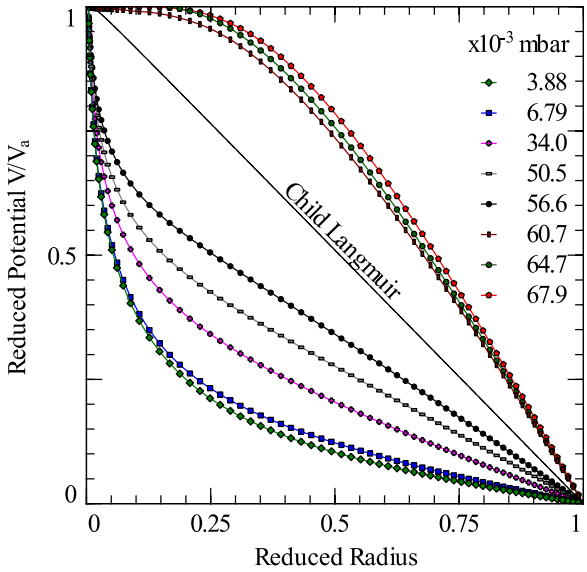

Figure 8. Child–Langmuir limit for the pressure of mode transition and PIC simulations' reduced potential V/V_A at $z = z_m$ against reduced radius r/R_c for various gas pressures. When increasing pressure, the positive space charge builds up near the anode. Above a given pressure, the voltage profile crosses the one obtained from Child–Langmuir model and transition occurs. Potential is then flattened near the anode to sustain higher currents.

more important than electron ones in the vicinity of the mode transition. Charged particles are thus mainly ions, justifying the study of the discharge as a space-charge-limited ion current between electrodes. Nevertheless, ion neutral cross sections for elastic and charge exchange processes in helium ($\sigma \sim 2 \times 10^{-19}\,\mathrm{m}^2$) indicate that, at the pressure of transition, a typical ion has approximately five collisions on its way to the cathode. Collisions limit ion speed, increasing space charge and in turn limiting the sustainable current. Consequently, accounting for collisions is important to model the transition.

Thus, assuming an ion current between cylindrical electrodes, and using the collision frequency to model ion impacts, the Child–Langmuir problem can be stated as

$$\frac{\mathrm{d}}{\mathrm{d}r}\left(r\frac{\mathrm{d}V}{\mathrm{d}r}\right) = -\frac{I}{2\pi\epsilon_0 L v}, \tag{2}$$

$$mv\frac{\mathrm{d}v}{\mathrm{d}r} = -e\frac{\mathrm{d}V}{\mathrm{d}r} - \nu m v, \tag{3}$$

(2) and (3) being Poisson's equation expressed in cylindrical coordinates and the momentum equation for helium ions, respectively. Here V is the electric potential, v is the ion speed, I is the discharge current, L is the discharge length, m is the helium ion mass, e is the elementary charge and $\nu = \sigma n_g v$ is the ion collision frequency. Resolving numerically the system formed by (2) and (3) for ions having a thermal velocity at the anode with

$$\begin{matrix} V(R_a) = V_a \\ V(R_c) = 0 \end{matrix} \qquad E(R_a) = -\frac{\mathrm{d}V}{\mathrm{d}r}(R_a) = 0 \tag{4}$$

yields the Child–Langmuir limiting current I_{CL} for the studied configuration—anode potential and electrode geometry. I_{CL} is obtained when the space charge cancels the electric field at the anode, meaning that no more ions could be drawn.

For comparison, in the analytic situation of a classical Child–Langmuir current between planar electrodes [32], I_{CL} is expressed as

$$I_{CL_{\parallel}} \propto \frac{V^{3/2}}{d^2}, \tag{5}$$

where d is the inter electrode gap and V is the applied voltage. In our situation, the Child–Langmuir limiting current is a function of V, the inter electrode gap δR as well as the pressure p due to the collisional term in (3):

$$I_{CL} = I_{CL}(V, \delta R, p). \tag{6}$$

Remembering that the discharge voltage decreases with pressure, the discharge mode transition for a given current I_0 can be explained as follows. Figure 8 shows the reduced potential V/V_a versus reduced radius (r/R_c) at $z_m = L/2$ on a wide range of pressure values obtained from PIC simulations, as well as the Child–Langmuir limit obtained using the pressure $p = p_t$ of mode transition in the collisional term. At low pressure, the discharge voltage is high enough compared with the inter electrode gap δR to collect $I_0 < I_{CL}(V, \delta R, p_t)$. When increasing pressure, thus decreasing voltage, the discharge voltage reaches V_t, the computed Child–Langmuir potential for I_0 and δR, so that $I_0 = I_{CL}(V_t, \delta R, p_t)$. Above this pressure, it is no longer possible to sustain the discharge current I_0 without reducing the sheath width. Transition occurs and a space charge builds up near the anode. Grounded end plates push electrons away, favouring space charge build-up close to the longitudinal mid plane. This space charge flattens the radial potential profile near the anode, in turn decreasing the sheath width and hence permitting stronger current. Flat behaviour of the potential at $z \sim z_m$ near the anode observed in figure 9 creates a longitudinal confinement of electrons near the mid plane. Electrons therefore oscillate longitudinally close to z_m, increasing in turn the number density and confinement in that area. The plasma is no longer uniform longitudinally, but centred near the mid plane defined by $z = z_m$. This longitudinal constriction justifies the fact that

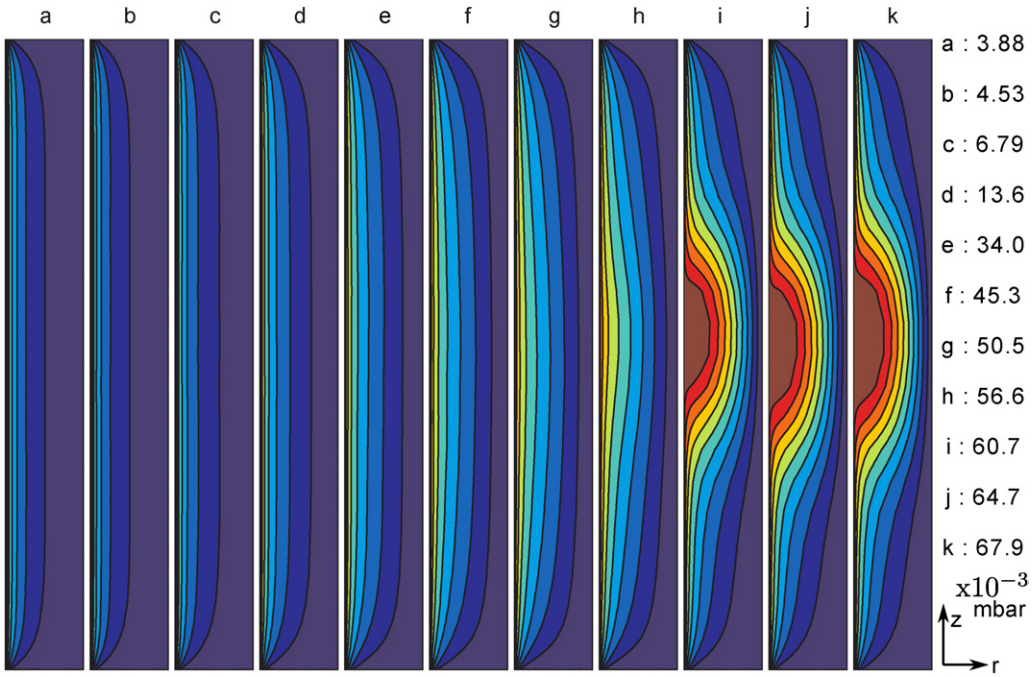

Figure 9. Evolution of the normalized electric potential distribution in the (r, z) plane with pressure. The formation of the electron confinement area existing in the diffuse mode is clearly seen.

Table 3. Comparative of experimental, simulation and Child–Langmuir model results for mode transition prediction.

	Experimental	Child–Langmuir model	Simulation
Transition voltage (V)	415	320	330
Sheath width (mm)	—	12	14

diffuse mode sheath width has a minimum. Indeed, working at constant current $I = 2\pi r L j(r)$, a longitudinal collapse induces an increase in $j(r)$. To sustain this current density rise without increasing the potential drop across the sheath, a step decrease in the sheath width is necessary.

Using this modified Child–Langmuir model, it is possible to predict the voltage of the mode transition for a given electrode geometry and discharge current. Moreover, knowing the voltage drop across the transition, we can calculate the sheath width of the *diffuse* mode and vice versa. Results obtained from experimental measurements, simulations and Child–Langmuir model are compared in table 3. Data show fair agreements and confirm the efficiency of the modified Child–Langmuir model for mode transition prediction.

To summarize, the mode transition is the result of a positive space charge growth beyond the threshold value, inducing a space-charge-limited regime. Transition is observed when current exceeds the Child–Langmuir current computed for the given configuration. The decrease in the mode transition pressure p_t noted in section 4 is the direct consequence of the accelerated build-up of positive space charge, higher value of secondary emission coefficient inducing higher electron number density n_e. Indeed, n_e being many times lower than the ion number density n_i near the mode transition, a small increase in n_e will induce a larger increase in n_i, and consequently the positive space charge limit for mode transition will be obtained at lower pressure.

Phenomenologically speaking, potential profiles given in figure 8 provide a new feature differencing the constricted and diffuse modes: the existence of an electric field at the anode. Following Donko's [33] proposition of definition of an obstructed discharge—the electric field does not vanish at the anode, the constricted mode could be an obstructed discharge mode between coaxial cylinders.

5.2. *Discharge voltage dependence on pressure*

For WIPS-based technologies, working conditions should exclude regions of $V-p$ curve divergence. Indeed divergence of the $V-p$ curve at a given current requires higher power input, which is to be avoided as much as possible. It is therefore important to get insights into the discharge voltage behaviour.

The wire cylinder configuration permits low pressure gaseous discharge at low discharge voltage. Indeed, although $V-p$ curves look like typical Paschen's curves, discharge can be operated at pressure orders of magnitude lower than that which would predict Paschen's law for a parallel plates configuration and a given potential. Even though the generalization of Paschen's law to non-uniform electric field between coaxial cylinders [34, 35] induces slight modifications, it cannot explain the low voltage ignition. Actually, due to the small anode radius used in our configuration, a large fraction of electrons misses the anode and orbits around it. The effective electron path for ionization is therefore much longer than the distance an electron would travel if it falls directly on the anode (hypothesis implicitly used for the derivation of Paschen's law between coaxial

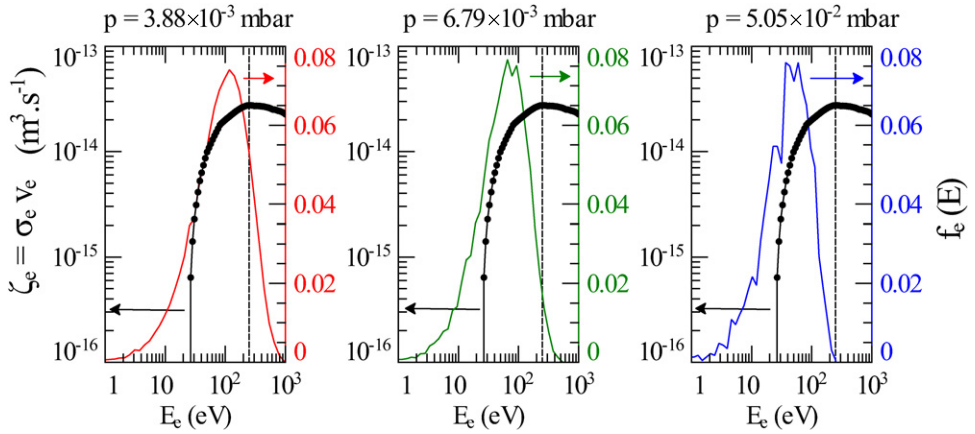

Figure 10. EEDF is plotted for different pressures along with the reduced electron ionization impact frequency $\zeta_{e^-} = \sigma^i_{e^-}(v_{e^-})v_{e^-}$ obtained from cross section.

cylinders). The direct consequence of this longer electron path is the capability to satisfy the breakdown criterion at much lower pressure, making it possible to operate discharges at 1 kV for pressure orders of magnitude lower than that which would predict Paschen's law [34]. To summarize, the observed deviation from Paschen's law results from the use of a very small anode.

The study of the V–p curve divergence relies on the electron population number N_e balance in the discharge. Considering that the anode current I is an electron current, the electron population number conservation can be expressed as

$$\frac{dN_e}{dt} = n_g \sum_{j=1}^{N_e} \zeta^j_{e^-} - I/e, \tag{7}$$

where $\zeta^j_{e^-} = \sigma^i_{e^-}(v^j_{e^-})v_{e^-j}$ is the reduced ionization frequency—ionization collision rate over number density—for the jth electron, N_e is the total number of electrons in the discharge, $v^j_{e^-}$ is the speed of the jth electron, $\sigma^i_{e^-}$ is the ionization cross section for electron impact and n_g is the neutral gas density. Secondary emission of electrons from ions and fast neutrals' impact on the cathode should have been included in (7). Nevertheless, our interest here is in the low-pressure range where secondary electrons are mainly impacting back on the cathode after crossing the discharge chamber without collisions. We thus neglect both secondary emission of electrons and electron current at the cathode, which are supposed to balance each other. Ion and fast neutral impact ionization phenomena, which are found to be of second order, have been neglected as well.

Introducing the mean reduced electron ionization rate ζ_m and the anode electron collection rate ν_a as

$$\zeta_m = \frac{1}{N_e} \sum_{j=1}^{N_e} \zeta^j_{e^-} \tag{8}$$

and

$$I = eN_e\nu_a, \tag{9}$$

equation (7) becomes

$$\frac{dN_e}{dt} = N_e(n_g\zeta_m - \nu_a). \tag{10}$$

At steady state, $n_g\zeta_m = \nu_a$. In addition, anode current I and set point current I_0 have to be equal, so $n_g\zeta_m = \nu_a|_{I=I_0} = \nu_{a_0}$. Hence, a pressure decrease has to be compensated by an increase in ζ_m or a decrease in ν_{a_0}.

As shown in figure 10, $d\zeta_{e^-}/dE_e$ decreases with electron energy E_e, becoming negative above threshold value E_{e_T}—energy for which ζ_{e^-} is maximum. Therefore, for an individual electron, increasing ζ_{e^-} by $\Delta\zeta_{e^-}$ requires a larger ΔE_e as E_e increases, until it gets impossible ($E_e \geqslant E_{e_T}$). Generalizing to the whole electron population, ζ_m has a qualitatively similar behaviour, exhibiting a maximum as the electron energy distribution function (EEDF) peaks around E_{e_T}. As featured in figure 11, electron mean energy varies almost linearly with the discharge voltage in the constricted mode. Consequently, behaviour of ζ_m as a function of electron mean energy or discharge voltage is identical. This behaviour is well illustrated by the EEDF obtained from PIC simulations (see figure 10). At higher pressure, electron temperature is low and a voltage increase results in the increase in the ionization cross section of all electrons, leading to a large increase in ζ_m. When pressure decreases, due to the combined effect of a lower slope of $\zeta_{e^-}(E_e)$ and an increase in the fraction of electrons having an energy above E_{e_T}, $\partial\zeta_m/dV$ decreases. Decreasing further the pressure will lead ζ_m to reach a maximum and then to decrease.

On the other hand, ν_{a_0} can be seen as a measure of the electron confinement. The lower ν_{a_0}, the better is the confinement. On the lower voltage range, ν_{a_0} remains almost constant as low primary electron energy leads mainly to isotropic scattering. As voltage increases, higher electron mean temperature leads to a smaller angle of scattering and higher energy for secondary electrons. Smaller scattering angles allow primaries to keep on their path and miss the anode. Higher energy for secondaries increases their chance to miss the anode. Hence ν_{a_0} is a decreasing function of the electron mean energy and, in turn, of voltage. Scattering models [19] show that the higher the electron energy E_e, the higher is the ΔE_e required to decrease the angle of scattering or increase the energy of secondaries by a given value. Therefore, after passing through a maximum, $|\partial\nu_{a_0}/\partial V|$ decreases with electron energy or anode potential.

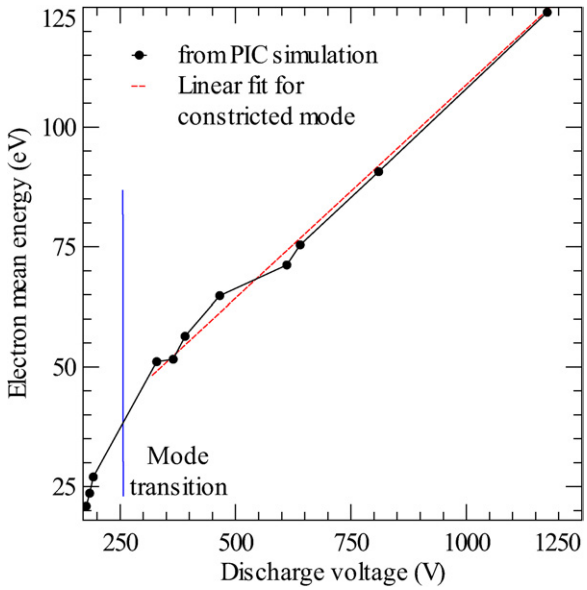

Figure 11. Electron mean energy versus discharge voltage obtained from PIC simulations. Data corresponding to the constricted mode are well fitted by a linear curve (red dashed curve).

Evolution of ζ_m, ν_a and N_e with a diminution of pressure is obtained from time constants of the various processes involved. As pressure is decreased, the anode current I and thus ν_a diminish in a fraction of $\tau = (n_g\zeta_m)^{-1}$—the inverse of the ionization rate. Then, as I is lower than set point value I_0, a positive charge builds up on the anode and, in turn, the anode potential rises as $(I_0 - I)t$ until I return to I_0. As anode potential increases, ζ_m evolves in about the time it takes for an electron to make one orbit around the wire. This period is about 10^{-8} s for an electron of a few hundred electronvolts, being smaller than τ which varies from 8×10^{-8} to 7×10^{-7} s depending on pressure. Equation (7) shows that N_e evolution is slower, with a time constant of a few τ.

The evolution of $\partial V/\partial p$ can thus be summarized as follows. At higher pressure, the voltage increase ΔV needed to get a sufficient growth of ζ_m to balance the n_g decrease is small, and thus obtained quickly. Therefore, $(n_g\zeta_m - \nu_a)$ returns to zero before N_e had time to evolve. Besides, small ΔV at low discharge voltage leaves ν_{a_0} unchanged, so during the short transient regime ν_a decreases with I and then returns to almost the same ν_{a_0}. As pressure diminishes, $\partial\zeta_m/\partial V$ decreases, so a larger ΔV is needed. Charging of the anode to get this larger ΔV takes longer, leaving enough time for a growth of N_e. In the meantime, ν_{a_0} starts decreasing as discharge voltage rises. Decreasing further the pressure, ζ_m is less capable of balancing alone a decrease in n_g, which is then compensated by a proportional decrease in ν_{a_0}. $|\partial\nu_{a_0}/\partial V|$ being decreasing, V–p curve divergence initiated by the ζ_m saturation is extended at low pressure.

Since ν_{a_0} is proportional to the neutral number density at low pressure, $N_e = I_0(e\nu_{a_0})^{-1}$ has to increase as $1/n_g$. This is confirmed by simulated data shown in figure 7. As pressure increases, n_g decrease is mainly compensated by an increase in ζ_m, and N_e decreasing rate tends to zero.

To prevent divergence, and thus extend the optimal range of working conditions, McClure [1] proved experimentally that a solution was to decrease the anode radius or end plates holes' radii. As shown in table 4, simulations confirm efficiency of both methods. We already explained how smaller wire radii yield better ionization efficiency (or similarly lower ν_{a_0}) and thus lower discharge voltage. On the other hand, smaller end apertures lead to better confinement of electrons. This improved confinement allows higher electron density without voltage increase. Looking at figure 7, this indeed means translating the point of the V–p curve divergence to lower pressures.

Table 4. Simulated discharge voltage for various anode radii (R_a) and end plates holes radii (R_{end}) for $p = 3.88 \times 10^{-3}$ mbar.

		R_a (μm)	
		75	100
R_{end} (mm)	1.5	—	1130 V
	3	1115 V	1175 V

6. Summary

In this paper, a 2D3v PIC code was used to study a wire discharge and its mode transition. Simulations reproduce fairly well the two discharge modes and their distinct properties—e.g. glow intensity and discharge voltage. Longitudinal constriction and voltage drop at the mode transition match closely the experimental data.

The simulation results justify modelling the discharge near the mode transition as a unipolar ion current between cylindrical electrodes and allow us to conclude that the diffuse mode is a space-charge-dominated regime. A modified Child–Langmuir law accounting for collisional effects is proposed, and its ability to predict mode transition is successfully validated against experimental and PIC results. Discharge voltage dependence on pressure is satisfactorily explained in light of electron ionization frequency variations.

Despite a close match in terms of relative intensity levels, glow longitudinal profiles of the diffuse mode obtained from experiments and simulations for various operating conditions differ slightly, experimental profiles being a little wider. Diffusion of light on the electrodes was mentioned as a plausible contributor to that profile broadening, de-excitation of the helium metastable states being possibly another one. To go further, the addition of a collisional radiative module to the existing code would permit distinguishing between the various excited states and thus allow us to, among other things, discriminate the influence of metastable states on emission profiles.

References

[1] McClure G W 1963 *Appl. Phys. Lett.* **2** 233–4
[2] Kingdon K H 1923 *Phys. Rev.* B **21** 408–18
[3] Pigache D and Fournier G 1975 *J. Vac. Sci. Technol.* **12** 1197–9
[4] McIlraith A 1966 *Nature* **212** 1422
[5] Urai H, Hotta E, Maeyama M S, Yasui H and Tamagawa T 1994 *Japan. J. Appl. Phys.* **33** 4243–6

[6] Yasui H, Tamagawa T, Ohshima I, Urai H and Hotta E 1995 *Radiat. Phys. Chem.* **46** 499–502
[7] Urai H, Kurosawa T, Okino A, Hotta E, Yasui H, Tamagawa T and Ko K C 1997 *Rev. Sci. Instrum.* **68** 3346–50
[8] Chalise P R, Watanabe M, Okino A, Ko K and Hotta E 2003 *Plasma Sources Sci. Technol.* **12** 235–43
[9] Makarov M, Loumani Y and Kozyrev A 2006 *J. Appl. Phys.* **100** 033301
[10] Makarov M, Loumani Y, Minea T, Gousset G and Kozyrev A 2006 *Europhys. Lett.* **74** 431–7
[11] Minea T M, Loumani Y, Makarov M and Gousset G 2007 *Plasma Processes Polym.* **4** S973–7
[12] Pigache D 1987 *Proc. 18th Int. Conf. on Phenomena in Ionized Gases (Swansea, UK)* vol 4 pp 782–3
[13] Rushton G J, O'Shea K R and Fitch R K 1973 *J. Phys. D: Appl. Phys.* **6** 1167–72
[14] Hotta E, Suzuki M, Yasui H and Tamagawa T 1991 *Proc. IEEE Int. Conf. on Plasma Science (Williamsburg, VA)* p 198
[15] Mohamed A, Pot T and Chanetz B 1995 *Int. Congress on Instrumentation in Aerospace Simulation Facilities (Dayton, OH)* pp 14.1–14.4
[16] Francis G 1956 The glow discharge at low pressure *Encyclopedia of Physics* (Berlin: Springer)
[17] Dawson J M 1983 *Rev. Mod. Phys.* **55** 403–47
[18] Birdsall C and Langdon A 1985 *Plasma Physics via Computer Simulation* (New York: McGraw-Hill)
[19] Birdsall C K 1991 *IEEE Trans. Plasma Sci.* **19** 65–85
[20] Hartmann P, Donko Z, Bano G, Szalai L and Rozsa K 2000 *Plasma Sources Sci. Technol.* **9** 183–90, ISSN 0963-0252
[21] Stone P M, Kim Y K and Desclaux J P 2002 *J. Res. Natl Inst. Stand. Technol.* **107** 327–37
[22] Surendra M, Graves D B and Jellum G M 1990 *Phys. Rev.* A **41** 1112–25
[23] Opal C B, Peterson W K and Beaty E C 1971 *J. Chem. Phys.* **55** 4100–6
[24] Skullerud H R 1968 *J. Phys. D: Appl. Phys.* **1** 1567–8
[25] Kaminsky M 1965 *Atomic and Ionic Impact Phenomena on Metal Surfaces* (Berlin: Springer)
[26] Katz I, Parks D E, Mandell M J, Harvey J M, Brownell D H J, Wang S S and Rotenberg M 1977 A three dimensional dynamic study of electrostatic charging in materials *Technical Report* NASA-CR-135256; SSS-R-77-3367
[27] Bohm C and Perrin J 1993 *Rev. Sci. Instrum.* **64** 31–44
[28] Szapiro B, Rocca J J and Prabhuram T 1988 *Appl. Phys. Lett.* **53** 358–60
[29] Vaughan J 1989 *IEEE Trans. Electron Devices* **36** 1963–7, ISSN 0018-9383
[30] Scholtz J J, Dijkkamp D and Schmitz R W A 1996 *Philips J. Res.* **50** 375–89, ISSN 0165-5817
[31] Furman M A and Pivi M T F 2002 *Phys. Rev. ST Accel Beams* **5** 124404
[32] Langmuir I 1913 *Phys. Rev.* **2** 450–86
[33] Donko Z, Rózsa K, Tobin R C and Peard K A 1994 *Phys. Rev.* E **49** 3283–9
[34] Druyvesteyn M J and Penning F M 1940 *Rev. Mod. Phys.* **12** 87–176
[35] Von Engel A 1954 *Ionized Gases* (New York: American Institute of Physics)